

# Theoretical Study on the Degree of CO<sub>2</sub> Activation in CO<sub>2</sub>-Coordinated Ni(0) Complexes

Joonho Park,\* Moses Cho, Young Min Rhee, and Yousung Jung

Cite This: *ACS Omega* 2021, 6, 7646–7654

Read Online

ACCESS |



Metrics &amp; More



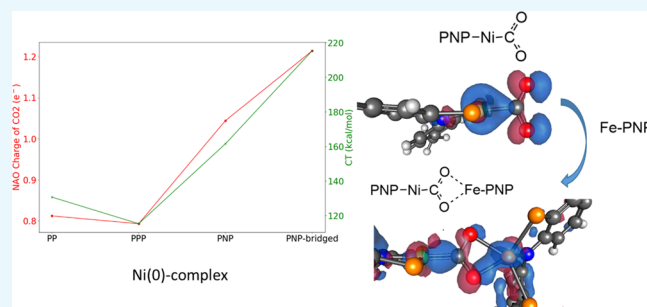
Article Recommendations



Supporting Information

**ABSTRACT:** The geometrical characteristic and the degree of CO<sub>2</sub> activation of the CO<sub>2</sub>-coordinated Ni(0) complexes were investigated computationally by quantum chemical means for bidentate and tridentate ligands of PP, PP<sup>Me</sup>P, and PNP, and sometimes with co-complexing Fe(II) to differently coordinate CO<sub>2</sub>. We show that the coordination geometry of the central metal is determined by the ligand geometry. The charge and the energy decomposition analyses show that the charge transfer energy through orbital mixing has a strong correlation with CO<sub>2</sub> net charge, while the binding energy cannot due to the lack of the coordination number and the deformation energy of the ligand.

Among the examined ligands, PNP with negatively charged secondary amine makes Ni(0) an electron-rich atom, which results in an ~20% higher CO<sub>2</sub> activation than those of PP and PP<sup>Me</sup>P. In particular, Fe(II)-PNP in the CO<sub>2</sub>-bridged diatomic complex enhances CO<sub>2</sub> activation by another ~20%, partly through the inductive effect of Fe(II), which pulls electron density from Ni-PNP across the CO<sub>2</sub>-bridge and partly by the backward donation from Fe(II)-PNP. Therefore, the present study encourages us to design a strongly electron-donating ligand and a CO<sub>2</sub>-bridged diatomic complex to develop more efficient homogeneous catalyst.



## I. INTRODUCTION

As human civilization has continued to develop, energy consumption has increased exponentially, especially after the industrial revolution. Because this energy demand has mostly been met by burning carbonaceous fossil fuels such as oil, coal, and natural gas, the liberated carbon has increased the CO<sub>2</sub> level in the air, which is believed to be responsible for global warming and the ongoing climate disaster on this planet.<sup>1</sup> As a result, developing renewable energies and related technologies for environmental protection has become an urgent and imminent issue. Although there are diverse approaches to mitigate the CO<sub>2</sub> level in the atmosphere, the most promising strategy is to reduce CO<sub>2</sub> to any form of a valuable material because carbon itself is also a necessary resource for energy circulation and sustaining the framework of organic substances.<sup>2</sup> By chemical reduction, depending on the reduction pathway and the degree of reduction, CO<sub>2</sub> is converted into an energy resource such as CO, methanol, or methane. In the full pathway of CO<sub>2</sub> reduction, the first reduction step of CO<sub>2</sub> + e<sup>-</sup> → CO<sub>2</sub><sup>-</sup> shows the highest activation barrier of 1.9 eV.<sup>3</sup> Inevitably, this higher activation barrier necessitates the assistance of the catalyst toward decreasing the energy cost in the CO<sub>2</sub> reduction.

There have been many developments in finding catalysts for CO<sub>2</sub> activation in the areas of both homogeneous<sup>4</sup> and heterogeneous catalysis.<sup>5</sup> Regardless of the area, to understand the nature of CO<sub>2</sub> in the activated form with the characteristics of the catalysts themselves will be important in developing new

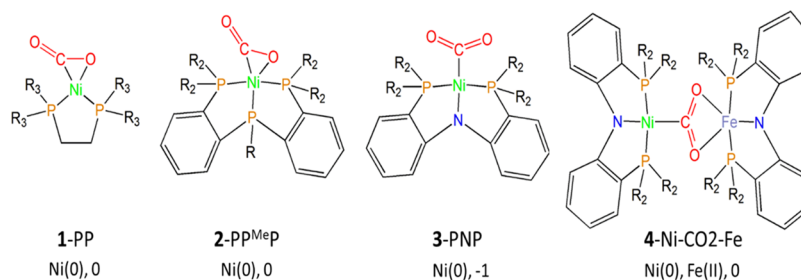
strategies of activating CO<sub>2</sub>.<sup>6</sup> In the homogeneous area, the molecular catalyst is solvated in a solution, normally in water, and it takes part in a catalyzing reaction in free solution or by being bound on the electrode surface. These catalysts are conventionally composed of a central metal (M), normally a transition metal (TM), and surrounding ligands. Carbon dioxide then adds to a vacancy in a metal atom or replaces a loosely bound ligand for further reaction. Many combinations of diverse metals and ligands have been studied in detail.<sup>7</sup> Among them, Ni-cyclam<sup>8–12</sup> (cyclam = 1,4,8,11-tetraazacyclotetradecan) and Fe- and Co-porphyrin families<sup>7</sup> have shown interesting behaviors in terms of their performance and chemical mechanisms. Particularly in the cyclam series, [Ni(II)(cyclam)]Cl<sub>2</sub> showed superior performance to those of Co<sup>2+</sup> and Fe<sup>2+</sup> with a low bias of -1.05 V and higher CO selectivity.<sup>9,10</sup> A mechanistic study by Song et al.<sup>8</sup> revealed that Ni(II)(cyclam) is first bound to the electrode surface and reduced by one electron with -1.07 V (experimentally -1.23 V),<sup>12</sup> Ni(I)(cyclam). This step is followed by thermoneutral CO<sub>2</sub> binding where CO<sub>2</sub> is reduced by one electron and Ni(I)

Received: December 24, 2020

Accepted: February 12, 2021

Published: March 8, 2021



Scheme 1. Schematic Presentation of Four Models<sup>a</sup>

<sup>a</sup>The metallic oxidation number and total charge are denoted. R, R<sub>2</sub>, and R<sub>3</sub> represent the methyl, isopropyl, and isobutyl groups, respectively.

is oxidized to Ni(II). In the whole catalytic reaction, the role of Ni(I) is crucial, as CO<sub>2</sub> is attached to Ni(cyclam)<sup>+</sup>. Also, the amount of charge moving from Ni(I) to CO<sub>2</sub> in this step would control the feasibility of the whole reduction mechanism.

The effect of the ligand was further studied experimentally by substituting H with a methyl group in the secondary amine position of the cyclam. The substitution lowered the overpotential compared to the pristine Ni(cyclam)<sup>2+</sup>, but it enhanced the Gibbs energy of CO<sub>2</sub> binding, which overall decreased the catalyst performance.<sup>8</sup> The performance deterioration was ascribed to the thermodynamic stability of the CO<sub>2</sub> adduct and its steric hindrance. Even though important insights have been drawn from these studies, many questions remain with regard to the characteristics of ligands (e.g., steric and/or inductive effect, roles of anchor atoms such as N, P, and S) and the central metals (e.g., the shape of d- and f-orbitals, HOMO-LUMO energy gap, and the oxidation state). In the case of polydentate ligands, the coordination bond between the central metal and the coordinating atoms can be strained and affect the catalytic role.

Because the state of the central metal, Ni(I) in cyclam rather than Ni(II), is crucial for CO<sub>2</sub> reduction, as stated above,<sup>8</sup> the study for the low-valent metal-CO<sub>2</sub> adducts has attracted much interest. After the characterization of (PCy<sub>3</sub>)<sub>2</sub>Ni(η<sup>2</sup>-CO<sub>2</sub>)<sup>13</sup> (Cy = cyclohexyl) with zero-valent Ni, referred to as Ni<sup>0</sup>, many Ni-CO<sub>2</sub> adducts with low valency were compounded.<sup>14,15</sup> When the metal makes a coordination bond to C of CO<sub>2</sub>, Ni<sup>0</sup> with large electron density can act as a strong nucleophile. Therefore, it is expected that the lower valent Ni will reduce CO<sub>2</sub> much more and make it more feasible to reduce CO<sub>2</sub> to other materials.

Recently, Lee's group synthesized a series of CO<sub>2</sub>-coordinated Ni<sup>0</sup> complexes where each ligand has a denticity of two or three for each Ni<sup>0</sup> atom.<sup>16–19</sup> Therefore, it is very heuristic to investigate the nature of Ni<sup>0</sup>-CO<sub>2</sub> interaction systematically for this series. The models to be studied are represented in Scheme 1. The first model is (dtbpe)Ni-(η<sup>2</sup>-CO<sub>2</sub>) (dtbpe = 1,2-bis(di-*tert*-butylphosphino)ethane)<sup>14</sup> denoted by 1-PP, where dtbpe is a bidentate neutral ligand with two P's as anchor atoms. The second one is (PP<sup>MeP</sup>)Ni-(η<sup>2</sup>-CO<sub>2</sub>)<sup>16</sup> denoted by 2-PP<sup>MeP</sup>, where PP<sup>MeP</sup> (PMe[2-P<sup>i</sup>Pr<sub>2</sub>-C<sub>6</sub>H<sub>4</sub>]<sub>2</sub>, P<sup>i</sup>Pr<sub>2</sub> = di-*iso*-propylphosphino-) is the modification of PPP anion of bis(2-di-*iso*-propylphosphinophenyl)phosphide<sup>20</sup> as a tridentate ligand. Note that all P's are tertiary phosphine excluding coordination to Ni. The third one is (PNP)Ni-η<sup>1</sup>-CO<sub>2</sub>-κC (PNP = N[2-P<sup>i</sup>Pr<sub>2</sub>-4-Me-C<sub>6</sub>H<sub>3</sub>]<sub>2</sub>)<sup>19,21</sup> denoted by 3-PNP, where PNP is an anionic ligand of the charge of -1. Note that the middle N in PNP is a secondary amine with two

lone pairs, which results in a formal charge of -1. The fourth one is (PNP)Ni-μ-CO<sub>2</sub>-κC:κ<sup>2</sup>O,O'-Fe(PNP)<sup>18</sup> as denoted by 4-Ni-CO<sub>2</sub>-Fe, where two metal centers are bridged by CO<sub>2</sub>. This is a biomimetic complex of carbon monoxide dehydrogenase (CODH), which converts CO<sub>2</sub> and CO reversibly.<sup>22,23</sup> In the active site of CODH, CO<sub>2</sub> is bridged between two metal centers of Ni and Fe (Ni-μ-CO<sub>2</sub>-κC:κO-Fe), as shown in Figure S1. Some calculations have been performed for a hypothetical model, as shown in Scheme S1, which replaces the middle P in 2-PP<sup>MeP</sup> with the tertiary N, referred to as 2'-PN<sup>MeP</sup>, to understand the difference of the effects of the anchor atom species and its valence electrons. 2'-PN<sup>MeP</sup> resembles 2-PP<sup>MeP</sup> with respect to the shape of valence electrons while it has the same anchor atom species as 3-PNP. We try to analyze the structural characteristics and the degree of CO<sub>2</sub> activation for these models based on DFT calculations. For the estimation of the degree of CO<sub>2</sub> activation, the electron charge density of CO<sub>2</sub> is analyzed because the amount of electron charges on a CO<sub>2</sub> molecule would facilitate the CO<sub>2</sub> reduction reaction.

## II. COMPUTATIONAL RESULTS AND DISCUSSION

For theoretical investigation, the hybrid density functional of B3LYP/6-31G(d) with dispersion correction<sup>24</sup> equipped in Q-Chem<sup>25</sup> was applied for geometry optimization, and the triple zeta basis set of G3Large was used for energy calculation. Each model was fully optimized, and the natural bond orbital (NBO)<sup>26</sup> analysis was applied for the charge of metals (M = Ni, Fe) and CO<sub>2</sub>. The energy decomposition analysis (EDA)<sup>27</sup> was done between the fragments of CO<sub>2</sub> and the metal complex for each model. The charges and spin multiplicities used in the calculation are 0, 0 for Ni(0) and +2, 5 for Fe(II), and the overall charge of ligand PNP is -1, whereas all the other ligands are neutral.

**a. Analysis of Geometry.** The optimized structures are shown in Figure 1, and some geometrical parameters are summarized in Table 1. In Figure 1, H was removed, and C of ligands is drawn as a point for clear view. The full geometrical presentations including H are presented in Figure S2 in the Supporting Information.

Because there are so many CO<sub>2</sub> adsorption modes for a single-atomic and diatomic catalyst,<sup>4</sup> all the modes addressed in this work are presented in Figure S3. It is known that η<sup>2</sup>-C,O is the most stable for Ni<sup>0</sup> without any ligands.<sup>28</sup> The ground state of Ni<sup>0</sup> with the coordination of a ligand is a singlet state of d<sup>10</sup> (Table S1). As presented in the previous work,<sup>28</sup> 1-PP and 2-PP<sup>MeP</sup> have η<sup>2</sup>-C,O mode as shown in Figure 1. While many CO<sub>2</sub>-adducts appear as η<sup>2</sup>-mode, it is known that some CO<sub>2</sub>-adducts have η<sup>1</sup>-C mode when a metal is in a relatively

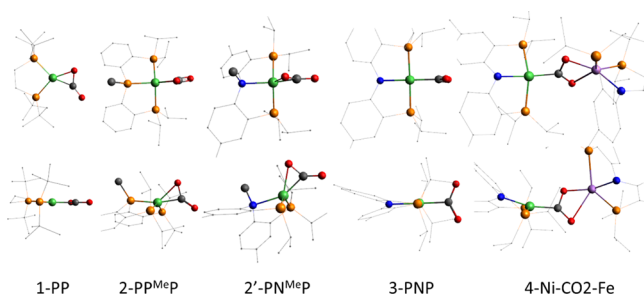


**Figure 1.** The optimized structures of five models in Scheme 1 and Scheme S1 are drawn with the top view (top) and side view (bottom) using B3LYP/6-31G(d) + D. H's are removed and some C's in ligands are drawn as points for clarity. Color scheme: Ni, green; P, brown; C, black; O, red; N, blue; Fe, violet.

low oxidation state so that the energy of the d-orbital is relatively high, as well as when a central metal has a square planar or square pyramidal structure.<sup>4</sup> Then, in 3-PNP, Ni<sup>0</sup> has square planar-like structure without CO<sub>2</sub>, which makes it prefer  $\eta^1$ -C mode, as shown in Figure 1. As for Fe(II) in model 4-Ni-CO<sub>2</sub>-Fe, it has  $\kappa^2$ O,O' mode with respect to CO<sub>2</sub>. Note that the charge of PNP-Fe is +1 as it is composed of Cl<sup>-</sup> in synthesis.<sup>17</sup> Hereafter, Ni(0)-PNP and Fe(II)-PNP without the coordination to CO<sub>2</sub> are simply denoted as Ni-PNP and Fe-PNP, respectively, without any complexity in notation. The calculation shows that Fe<sup>2+</sup> has a multiplicity of quintets with high spin in PNP-Fe, as shown in Table S2. All the charges and multiplicities of models in calculation are listed in Table 1.

The values with parentheses in Table 1 come from X-ray crystal structures. In this calculation regime, the coordination geometries of all the models are well reproduced except for 4-Ni-CO<sub>2</sub>-Fe, where two bulky PNP ligands are closely located and the calculation overestimates the dispersion correction, causing the ligands to become slightly twisted, as shown in Figure S4.

From 1-PP to 3-PNP, there is a systematic change of ligands. As for Ni<sup>0</sup> with two coordination to P's, there is an in-depth theoretical study with minimal monodentate ligands of two PH<sub>3</sub>, where two ligands have no geometrical constraint.<sup>29</sup> In the 1-PP model, although two ligands are connected by the ethyl group, the geometry with Ni and CO<sub>2</sub> is not much different from that with the two monodentate ligands. All the atoms of CO<sub>2</sub> lie in the molecular plane, as shown in Figure 1, as is the case with Ni(PH<sub>3</sub>)<sub>2</sub>.<sup>29</sup>

Moving to 2-PP<sup>Me</sup>P, the coordination number is increased to three with the tridentate ligand of PP<sup>Me</sup>P, where Ni has a Td-like structure with three P's and CO<sub>2</sub> in  $\eta^2$ -C,O mode. The CO<sub>2</sub> plane is perpendicular to the ligand plane, which is

composed of the three anchor atoms of the ligand. To understand the effect of the tridentate ligands on coordination geometries, three tridentate ligands are shown in Figure 2. The optimized structure of PP<sup>Me</sup>P is shown in Figure 2 a, where some valence orbitals are drawn with parity. Those orbitals mainly correspond to the lone pair electrons of the anchor atoms and are directed to above the ligand plane displayed with green triangle. Each MO is separately drawn in Figure S5. The directions of the lone pairs are ascribed to the sp<sup>3</sup> structure of the tertiary P as shown with the black arrow. Therefore, Ni can be located on top of the ligand plane, which results in the tetrahedral structure of Ni, as shown in Figure 1.

The effect of the substitution of the tertiary N for the middle P<sup>Me</sup> in PP<sup>Me</sup>P, referred to as PN<sup>Me</sup>P, is shown in Figure 2 b, where MOs are almost identical to PP<sup>Me</sup>P in Figure 2 a. Therefore, the geometry of the hypothetical model of 2'-PN<sup>Me</sup>P remains almost the same as 2-PP<sup>Me</sup>P, but the bond length of N-Ni and the angle of Me-N-Ni were decreased by about 0.05 Å and 25°, respectively, compared to 2-PP<sup>Me</sup>P due to the size and the electronegativity of N.

In 3-PNP, Ni-PNP makes a planar structure with  $\eta^1$ -C for CO<sub>2</sub>, where all the anchor atoms and Ni locate in the same plane together with C of CO<sub>2</sub>, as shown in Figure 1. The structure of ligand PNP and the four uppermost occupied MOs are shown in Figure 2 c, where MOs are located in the ligand plane. The two lone pairs of N are completely symmetric with respect to the ligand plane as shown in Figure S6, and the ligand shows the complete C<sub>2</sub> symmetry, as shown in Figure S7 a. Therefore, Ni<sup>0</sup> as well as Fe(II) is located in the ligand plane, making the Pl structure of Ni-PNP and Fe-PNP. From the ligand field theory, Ni<sup>0</sup> with a strongly donating ligand makes the electronic configuration of d<sup>10</sup>,<sup>10</sup> which leaves sp<sup>3</sup> orbitals for M-L (metal-ligand) coordination, resulting in a Td structure. Therefore, if the PNP ligand is replaced by three monodentate ligands such as two P(CH<sub>3</sub>)<sub>3</sub> and one [NH<sub>2</sub>]<sup>-1</sup>, it surely goes to a Td structure with  $\eta^2$ -C,O mode for CO<sub>2</sub> coordination, as shown in Figure 2 d. Therefore, although Ni<sup>0</sup> prefers a Td structure in its low oxidation state, when it is enforced to have a Pl structure, for example, due to the constraint of the chelating PNP ligand, it favors the  $\eta^1$ -C mode in CO<sub>2</sub> binding.

In 4-Ni-CO<sub>2</sub>-Fe, CO<sub>2</sub> is bridged by Ni-PNP and Fe-PNP in the type of  $\mu$ -CO<sub>2</sub>- $\kappa$ C: $\kappa^2$ O,O'. This molecule is prepared by two different metal complexes of Ni-PNP and Fe-PNP. Note that although the coordination structure of Fe-PNP is Pl in its optimized structure, it becomes Td in 4-Ni-CO<sub>2</sub>-Fe.

**b. Analysis of Electronic Structure.** To study the electronic properties of CO<sub>2</sub>-coordinated Ni<sup>0</sup> complexes, the energy levels and the atomic basis coefficients of molecular

**Table 1. Geometry Parameters for Models in Scheme 1 Using B3LYP/6-31G(d) + D<sup>a</sup>**

parameters	1-PP	2-PP <sup>Me</sup> P	3-PNP	4-Ni-CO <sub>2</sub> -Fe
chg. mul	0, 1	0, 1	-1, 1	0, 5
geometry Ni	Pl (Pl) <sup>14</sup>	Td (Td) <sup>16</sup>	Pl (Pl) <sup>19</sup>	Pl (Pl) <sup>18</sup>
d(C-O) (Å)	1.289, 1.212 (1.266, 1.200)	1.252, 1.224 (1.252, 1.217)	1.258, 1.257 (1.248, 1.247)	1.318, 1.255 (1.289, 1.269)
d(Ni-C)	1.811 (1.868)	1.875 (1.904)	1.880 (1.911)	1.844 (1.831)
d(Ni-O)	1.877 (1.904)	2.234 (2.191)	2.664 (2.614)	2.856, 2.575 (2.705, 2.772)
∠O-C-O(°)	137.8 (138.0)	133.4 (135.1)	129.6 (128.5)	118.4 (116.5)
d(Fe-O)				1.946, 2.503 (2.008, 2.289)
∠O-Fe-O(°)				58.0 (61.0)

<sup>a</sup>The values in parenthesis are given from crystallography. Pl and Td stand for planar and tetrahedral structures, respectively.

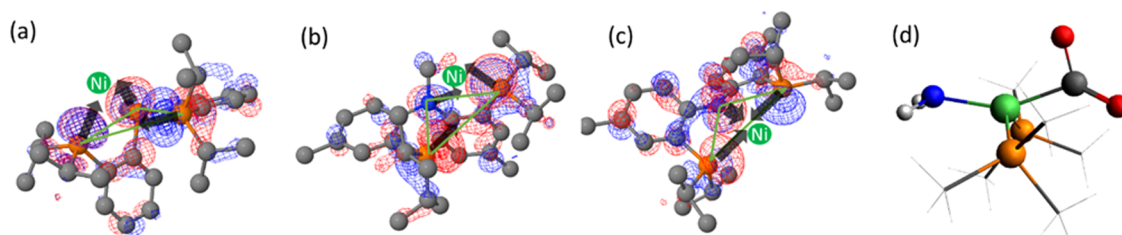


**Figure 2.** The optimized ligand structure of (a) PP<sup>MeP</sup>, (b) PN<sup>MeP</sup>, and (c) PNP, and (d) structure of [Ni(0)(PCH<sub>3</sub>)<sub>2</sub>NH<sub>2</sub>]<sup>-1</sup>-CO<sub>2</sub> calculated by B3LYP/6-31G(d) + D. In the ligand structures (a–c), H was removed for clarity. The black arrows denote the direction of the occupied molecular orbitals (MO) near the HOMO level, and the green triangle shows the ligand plane. The MOs in ligand structures are overlaid as much as the number of lone pairs. Colors scheme: Ni, green; C, gray; P, orange; N, blue; H, white; Fe, brown (drawn using Jmol).

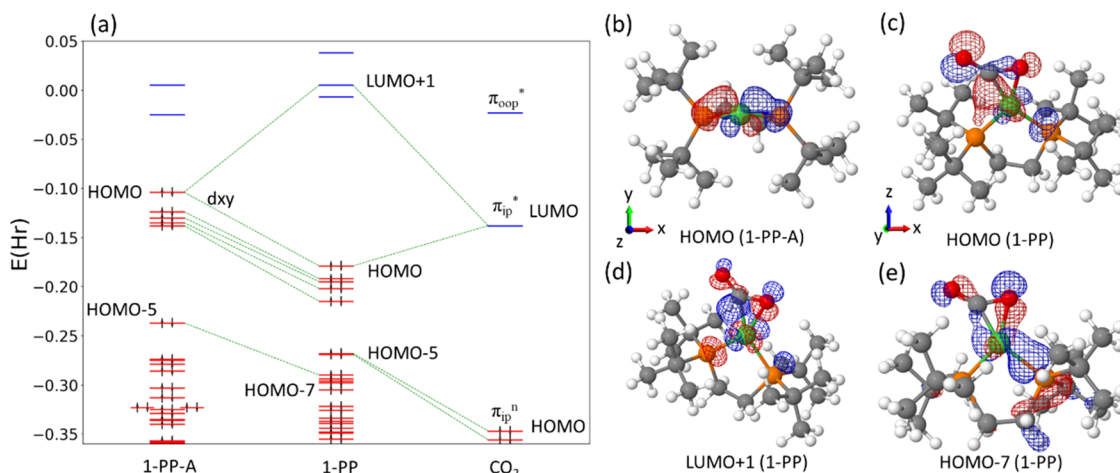


**Figure 3.** (a) MO levels of 1-PP and its fragments of 1-PP-A and CO<sub>2</sub> in fixed geometries. Only selected MOs are drawn, which are related to Ni and CO<sub>2</sub>. Representation of MOs of (b) HOMO of 1-PP-A (top view from z axis), (c) HOMO of 1-PP (side view from y axis), (d) LUMO+1 of 1-PP (slanted to view d<sub>xy</sub>-Ni), and (e) HOMO-7 of 1-PP. Colors scheme: Ni, green; C, gray; P, orange; N, blue; H, white (drawn using Jmol).

orbitals (MOs) were analyzed. The MO energy levels of 1-PP are shown in Figure 3a with its two fragments of CO<sub>2</sub> (right side) and the Ni complex (left side) referred to as 1-PP-A in their fixed geometries. When a free CO<sub>2</sub> is bent, the doubly degenerate HOMO ( $\pi_u^n$ , nonbonding orbital with 1 node) and LUMO ( $\pi_g^*$ , antibonding orbital with 2 nodes) levels are broken and the HOMO-LUMO gap is decreased as the HOMO level is increased and LUMO level is lowered, as shown in Figure S8. In the broken degeneracy, the MOs in the CO<sub>2</sub> plane, also called in-plane mode, take up LUMO ( $\pi_{ip}^*$ ) and HOMO ( $\pi_{ip}^n$ ), while the MOs perpendicular to them, also called out-of-plane mode, are located at LUMO+1 ( $\pi_{oop}^*$ ) and HOMO-1 ( $\pi_{oop}^n$ ). In Figure 3a, the red lines denote the occupied orbital levels, and the blue ones denote the unoccupied orbital levels. In Figure 3a, only the selected MO levels are drawn, which are related to the atomic orbitals of Ni and CO<sub>2</sub> for clarity. The green dashes denote the corresponding MOs between before and after CO<sub>2</sub> coordination, which can be just the energy shift or an orbital interaction. All the levels and the relaxed structures of both fragments are shown in Figure S9. From the relaxed geometry to the fixed geometry (1st → 2nd and 5th → 4th column in Figure S9), the occupied levels are raised and the unoccupied levels are lowered around HOMO and LUMO levels, which explains the energetically unstable structure due to geometrical deformation. In the binding of 1-PP-A and CO<sub>2</sub> in Figure 3a, the MO levels of Ni complex decrease while those of CO<sub>2</sub> increase. This large shift of the energy levels is ascribed to the charge transfer from Ni to CO<sub>2</sub>, where the electron–electron

repulsion energy is raised in CO<sub>2</sub> and lowered in Ni. The backward donation normally occurs through the orbital interactions between LUMO of the bent CO<sub>2</sub> ( $\pi_{ip}^*$ ) and any occupied orbitals of M complex, whereas the forward donation occurs through the orbital interactions between HOMO of the bent CO<sub>2</sub> ( $\pi_{ip}^n$ ) and any unoccupied orbitals of M complex if it exists. In 1-PP, HOMO of 1-PP-A interacts with  $\pi_{ip}^*$  of CO<sub>2</sub>, which means that the backward donation occurs dominantly and is responsible for the CO<sub>2</sub> activation.

The five occupied orbitals below HOMO in 1-PP-A mainly belong to Ni-3d orbitals but also include 4s, 4p orbitals due to the pre-existing coordination bond to P's. HOMO of 1-PP-A is mainly composed of d<sub>xy</sub>-Ni, as shown in Figure 3b. Note that the molecular ring is located on the xz plane. In Figure 3c,  $\pi_{ip}^*$ -CO<sub>2</sub> is well developed in HOMO of 1-PP, which comes from HOMO of 1-PP-A. Therefore, this demonstrates that d<sub>xy</sub>-Ni charges are moved to the empty CO<sub>2</sub> orbital, which confirms the backward donation of CO<sub>2</sub>. The correspondent antibonding appears in LUMO+1 as shown in Figure 3d, where the parity of CO<sub>2</sub> is changed compared to Figure 3c, while the parity of d<sub>xy</sub>-Ni remains the same. HOMO and HOMO-1 of the bent CO<sub>2</sub> are located at HOMO-5 and -6 in 1-PP, respectively, which are just the shift of MO levels primarily due to the electrostatic effect ascribed to the increased charge density. Some complicated interactions appear as shown in Figure 3d and Figure S10; however, no trace of the forward donation was detected through MO analysis, so the binding of CO<sub>2</sub> on Ni(0) occurs mainly through the backward donation.

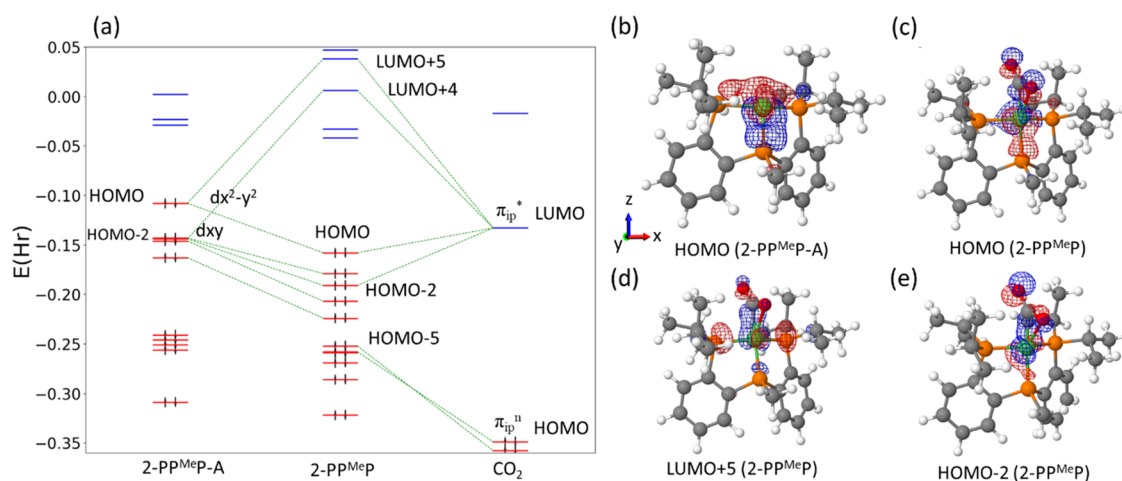


**Figure 4.** (a) MO levels of 2-PP<sup>Me</sup>P and its fragments of 2-PP<sup>Me</sup>P-A and CO<sub>2</sub> in fixed geometries. Only selected MOs are drawn, which are related to Ni, and C and O in CO<sub>2</sub>. Representation of MOs of (b) HOMO of 2-PP<sup>Me</sup>P-A, (c) HOMO of 2-PP<sup>Me</sup>P, (d) LUMO+5 of 2-PP<sup>Me</sup>P, and (e) HOMO-2 of 2-PP<sup>Me</sup>P. Colors scheme: Ni, green; C, gray; P, orange; N, blue; H, white (drawn using Jmol).

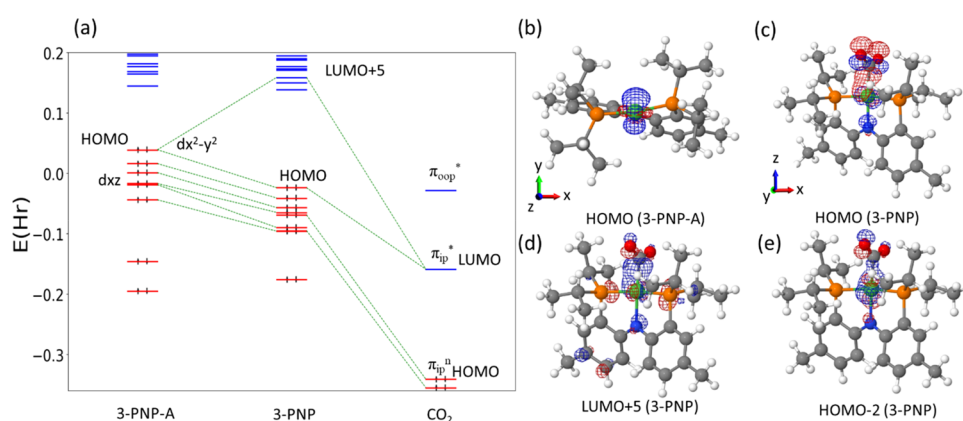


**Figure 5.** (a) MO levels of 3-PNP and its fragments of 3-PNP-A and CO<sub>2</sub> in fixed geometries. Only selected MOs are drawn, which are related to Ni and CO<sub>2</sub>. Representation of MOs of (b) HOMO of 3-PNP-A, (c) HOMO of 3-PNP, (d) LUMO+5 of 3-PNP, and (e) HOMO-2 of 3-PNP. Colors scheme: Ni, green; C, gray; P, orange; N, blue; H, white (drawn using Jmol).

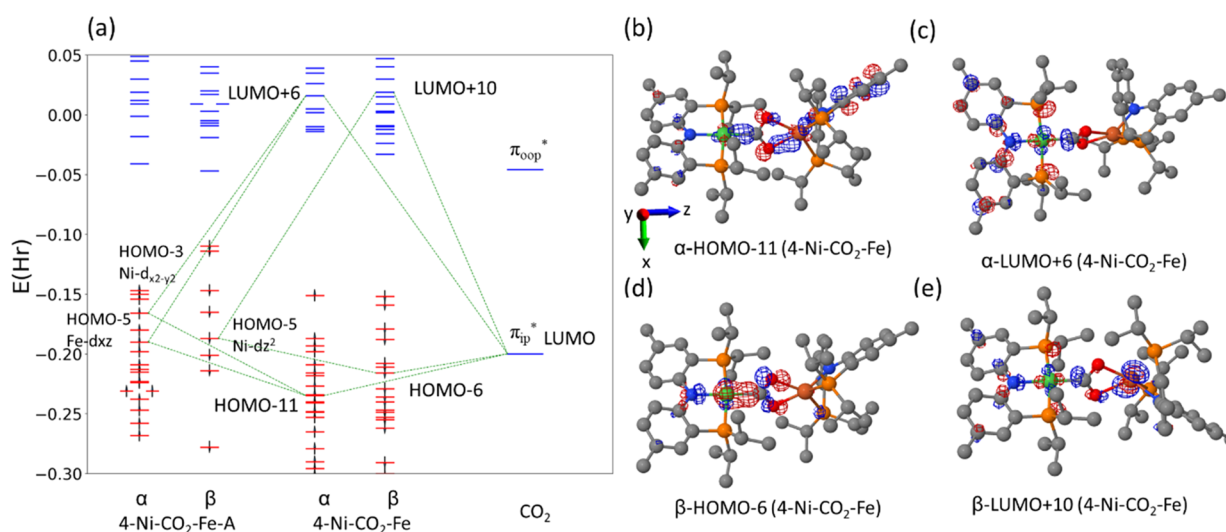


**Figure 6.** (a) MO levels of 4-Ni-CO<sub>2</sub>-Fe and its fragments of 4-Ni-CO<sub>2</sub>-Fe-A and CO<sub>2</sub> in fixed geometries. Only selected MOs are drawn, which are related to Ni, Fe, and C and O in CO<sub>2</sub>. Representation of MOs of (b) α-HOMO-11, (c) α-LUMO+6, (d) β-HOMO-6, and (e) β-LUMO+10 of 4-Ni-CO<sub>2</sub>-Fe. Colors scheme: Ni, green; Fe, brown; C, gray; P, orange; N, blue; H, white (drawn using Jmol).

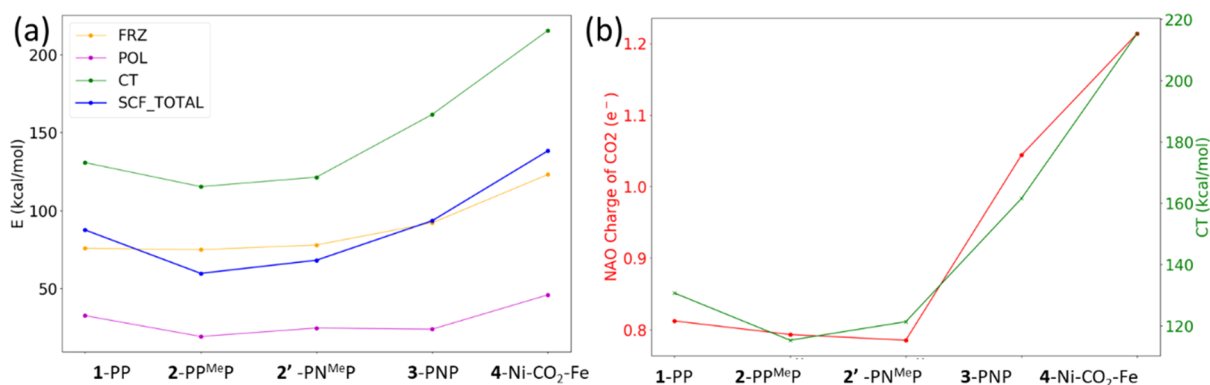


**Figure 7.** (a) Energy decomposition analysis (EDA). FRZ denotes frozen electron density, POL, polarization, CT, charge transfer, SCF\_TOTAL, the sum of CT, POL, and -FRZ. (b) Comparison between CO<sub>2</sub> charges from the natural atomic orbital and CT energy from EDA.

The MO levels of 2-PP<sup>MeP</sup> and its fragments of CO<sub>2</sub> and Ni complex (Ni-PP<sup>MeP</sup>-A) in fixed geometries are shown in Figure 4a, and there is not much difference from those of 1-PP. The overall molecular orbital levels including the relaxed geometries are also presented in Figure S11. In Figure 4a, there appears backward donation of CO<sub>2</sub> with  $d_{x^2-y^2}$  and  $d_{xy}$  in HOMO and HOMO-2 of 2-PP<sup>MeP</sup>-A, respectively. Then, the bonding and antibonding orbitals are shown in Figure 4c,d, and another backward donation at HOMO-2 in 2-PP<sup>MeP</sup> is detected Figure 4e.

The substitution of the tertiary P with the tertiary N for 2'-PN<sup>MeP</sup> does not make a significant difference, as shown in Figure S12, as expected through the similar valence electron structure. However, the secondary N-substitution effect on MO levels in 3-PNP is significant as shown in Figure 5a. The HOMO level of 3-PNP-A is much higher than the level of  $\pi_{ip}^*$ -CO<sub>2</sub>. This is ascribed to the raised HOMO level of 3-PNP-A due to the negatively charged N, while the level of  $\pi_{ip}^*$ -CO<sub>2</sub> stays at a similar energy level. The MO level difference between HOMO of 3-PNP-A and LUMO of CO<sub>2</sub> reaches 0.198 Hartree, which is much larger than those of 0.025–0.043 Hartree for the previous models. Therefore, this large energy difference can be a driving force for charge transfer from Ni complex to CO<sub>2</sub>. Due to the high energy of HOMO, PNP itself has a strong tendency to donate electrons when combined with any other molecule. Therefore, any M-PNP complex is expected to have a strong tendency to donate electrons when any molecule is coordinated to the central metal. Figure 5b shows HOMO of  $d_{x^2-y^2}$  of 3-PNP-A, which interacts with  $\pi_{ip}^*$ -CO<sub>2</sub>. The bonding and antibonding orbitals are drawn in Figure 5c,d, and another backward donation appear, as shown in Figure 5e.

Lastly, MO levels of the CO<sub>2</sub>-bridged bimetal complex of 4-Ni-CO<sub>2</sub>-Fe are presented in Figure 6a with those of its fragments in the fixed geometries. The green lines represent only the backward donations between metals and CO<sub>2</sub>. As for 4-Ni-CO<sub>2</sub>-Fe-A, two separate molecules of Ni-PNP and Fe-PNP exist, so they were calculated together as a supramolecule, as shown in Figure S14. The MO splitting in Figure 6a shows that both  $\alpha$ - and  $\beta$ -spin contribute to the backward donation to CO<sub>2</sub>. In the bonding orbital of  $\alpha$ -HOMO-11, two MOs from 4-Ni-CO<sub>2</sub>-Fe-A contribute, one from Ni (HOMO-3) and the other from Fe (HOME-5). The bonding and antibonding orbitals for  $\alpha$ -spin are drawn in Figure 6b,c. In the  $\alpha$ -bonding orbital, the C- $p_z$  orbital of  $\pi_{ip}^*$ -CO<sub>2</sub> bonds with Ni- $d_{x^2-y^2}$  while one of two O- $p_z$ 's of  $\pi_{ip}^*$ -CO<sub>2</sub> interacts with the Fe- $d_{xz}$  orbital.

Considering the parity of the Fe- $d_{xz}$  orbital and  $\pi_{ip}^*$ -CO<sub>2</sub>, only one O1- $p_z$  orbital (blue color) can overlap with the d-orbital of Fe (blue color) because the other O2- $p_z$  (blue color) has the opposite parity to Fe (red color), as shown in Figure 6b. Therefore, we can say that some portion of the backward donation can occur through the Fe-PNP complex when co-complexing CO<sub>2</sub> in  $\kappa^2$ O,O' mode. Note that the  $\alpha$ -spin is fully occupied in high spin of Fe<sup>2+</sup>, even though the d-orbital is not fully occupied. As for  $\beta$ -spin, the considerable backward donation appears only through Ni, as shown in Figure 6d. Because Fe<sup>2+</sup> has only one electron of  $\beta$ -spin in high spin configuration, no meaningful backward donation occurs from Fe<sup>2+</sup>. Resultantly, Fe(II)-PNP partly contributes to the backward donation to CO<sub>2</sub> in a concerted mode with Ni<sup>0</sup> in its high spin configuration.

**c. Charge and Energy Decomposition Analysis.** Energy decomposition analysis (EDA)<sup>27</sup> was done and displayed in Figure 7a for the five models in Scheme 1 and Scheme S1. In Figure 7a, FRZ of EDA components stands for the electrostatic repulsion energy attributed to the frozen electron density when two fragments of CO<sub>2</sub> and the Ni complex are combined in the fixed geometries. POL is the polarization energy through intrafragment relaxation from the frozen density, and CT is due to the interfragment electronic relaxation of MOs. Note that FRZ makes the system unstable while POL and CT make the system stable, so FRZ has an opposite sign. In Figure 7a, the sign of FRZ was reversed for comparison. The total SCF energy, referred to as SCF\_total in Figure 7a, is given by CT + POL - FRZ. FRZ (orange line) is increasing from 1-PP to 4-Ni-CO<sub>2</sub>-Fe, which means that the overlap interaction between two fragments is increasing. The POLs (violet line) of 1-PP and 4-Ni-CO<sub>2</sub>-Fe are higher than those of 2-PP<sup>MeP</sup> and 3-PNP, but their differences are relatively small compared to FRZ and CT. The large differences in the total SCF (blue line) mainly come from CT (green line) so both energies show a similar trend in Figure 7a. Roughly estimated, it looks like the relative energy differences between models in FRZ and POL counterbalance each other; thus, SCF resembles CT.

Therefore, the SCF energy is largely affected by the CT energy, which comes from the charge delocalization. Because the CO<sub>2</sub> binding occurs mainly through the backward donation, CT and BE are expected to be aligned. However, by definition, BE includes the deformation energy of each fragment with reference to the fully relaxed structures of each fragment, which is different from SCF\_TOTAL in EDA. BE in Figure S15a increases from 2-PP<sup>MeP</sup> to 4-Ni-CO<sub>2</sub>-Fe

Table 2. Partial Charges from Natural Atomic Orbital Analysis<sup>a</sup>

models	CO <sub>2</sub>	Ni <sup>0</sup>			Fe <sup>2+</sup>		
		Ni <sup>0</sup>	$\Delta_e$ Ni <sup>0</sup>	$\Delta_e$ (Ni <sup>0</sup> ,A's)	Fe <sup>2+</sup>	$\Delta_e$ Fe <sup>2+</sup>	$\Delta_e$ (Fe <sup>2+</sup> ,A's)
1-PP	-0.812	0.804	0.334	0.588	N/A		
2-PP <sup>Me</sup> P	-0.793	0.862	0.215	0.556	N/A		
3-PNP	-1.044	0.792	0.318	0.729	N/A		
4-Ni-CO <sub>2</sub> -Fe	-1.214	0.908	0.434	0.884	1.424	0.147	0.143

<sup>a</sup> $\Delta_e$ M and  $\Delta_e$ (M,A's) stand for the difference of atomic charges after CO<sub>2</sub> coordination for M and the sum of M and the anchor atoms (A's) of the ligand, respectively. The reference charges are 0.474 for Ni<sup>0</sup> and 1.277 for Fe<sup>2+</sup> in M complex without CO<sub>2</sub>.

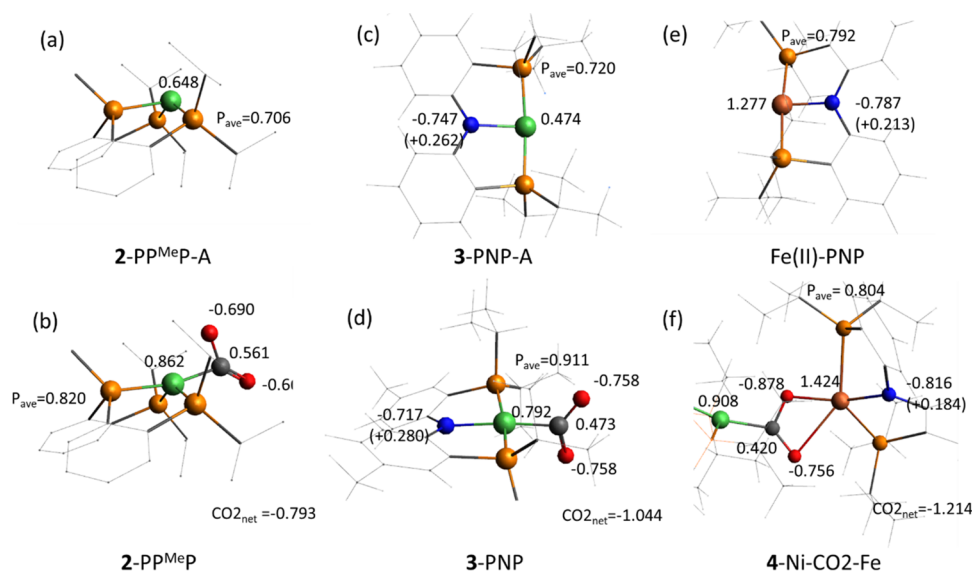


Figure 8. Atomic charges from natural atomic orbitals for (a) 2-PP<sup>Me</sup>P-A, (b) 2-PP<sup>Me</sup>P, (c) 3-PNP-A, (d) 3-PNP, (e) Fe-PNP, and (f) 4-Ni-CO<sub>2</sub>-Fe. Colors scheme: Ni, green; C, gray; P, orange; N, blue; Fe, brown.

smoothly. However, the abnormally high BE of 1-PP is ascribed to the lack of coordination bonds to Ni, which increased POL in Figure 7a. The difference between SCF and BE is much more for 4-Ni-CO<sub>2</sub>-Fe, where the coordination geometry of Fe-PNP changes greatly from PI to Td. This deformation energy abruptly reduced the BE of 4-Ni-CO<sub>2</sub>-Fe, which induces the inconsistency between BE and total SCF in this model series.

The natural atomic orbital (NAO) charge in natural bond orbital (NBO)<sup>26</sup> package was applied to measure the amount of charges on CO<sub>2</sub>, which can directly determine the degrees of CO<sub>2</sub> activation. The charges on CO<sub>2</sub> of NAO and CT of EDA show strong correlation in Figure 7b. The NAO charges on CO<sub>2</sub> are similar from 1-PP to 2-PP<sup>Me</sup>P but largely increase via 3-PNP to 4-Ni-CO<sub>2</sub>-Fe. This trend is similar to CT, which is represented by the green line in Figure 7b.

To quantitatively investigate the change of charges in the model series, NAO charges are analyzed as presented in Table 2, and all the atomic charges are in Table S3. The charge of M is the partial charge of M in each model.  $\Delta_e$ M and  $\Delta_e$ (M,A's) stand for the charge difference of M alone and the sum of M and its anchor atoms, respectively, between the cases before and after CO<sub>2</sub>-coordination. Some reference charges before CO<sub>2</sub> coordination are presented in Figure 8a,c,e and Table S3. The amount of the negative charge of CO<sub>2</sub> is around -0.80e in 1-PP and 2-PP<sup>Me</sup>P but increased to -1.04e in 3-PNP and -1.21e in 4-Ni-CO<sub>2</sub>-Fe. Note that as shown in Figure S16, the charge of CO<sub>2</sub> cannot be correlated with that of the central metal alone, but when it is summed with the charges of the

anchor atoms, some correlation appears. Therefore, from 1-PP to 2-PP<sup>Me</sup>P, CO<sub>2</sub> gets a little less charged, although Ni<sup>0</sup> becomes more positive. This is ascribed to the additional anchor atom, P, which is more electronegative (EN = 2.19) than Ni (EN = 1.91). The additional electronegative anchor atom would make the central atom less active for CO<sub>2</sub> activation. As for the PNP ligand, N has formal charge of -1 with two lone pair electrons that can donate charges to the next metal Ni(0) and Fe(II). As shown in Figure 8c, Ni in 3-PNP is less positive compared to 2-PP<sup>Me</sup>P in Figure 8a. Then, after CO<sub>2</sub> is coordinated, more electron charges on Ni can move to CO<sub>2</sub> by the amount of about 0.31e (3-PNP), compared to 0.21e in 2-PP<sup>Me</sup>P, which results in CO<sub>2</sub> activation of about -1.04e. As for the CO<sub>2</sub>-bridged diatomic complex of 4-Ni-CO<sub>2</sub>-Fe, the charge of CO<sub>2</sub> is increased to about -1.21e. First, from the Ni-PNP side, there is a positive charge increase, which means some electron charges are donated to CO<sub>2</sub>. Before adding Fe-PNP, the remaining part of 4-Ni-CO<sub>2</sub>-Fe is exactly the same as 3-PNP. Therefore, by coordinating Fe-PNP to 3-PNP as  $\kappa^2$ O,O' mode,  $\Delta_e$ (Ni<sup>0</sup>,A's) in 4-Ni-CO<sub>2</sub>-Fe is raised by 0.15e compared to that of 3-PNP, as shown in Table 2. It is very interesting that Fe<sup>2+</sup>, a strong Lewis acid can draw electron density from Ni-PNP across the CO<sub>2</sub> bridge, which means Fe<sup>2+</sup> strengthens the electron donation of Ni-PNP to CO<sub>2</sub>. On the other side,  $\Delta_e$ Fe<sup>2+</sup> of 4-Ni-CO<sub>2</sub>-Fe shows an increased charge of about 0.15e, as shown in Table 2, compared to the charge of Fe-PNP shown in Table S3. Considering that the sum of the charges of the anchor atoms is almost not changed, it can be interpreted like this. Fe<sup>2+</sup> in Fe-

PNP has relatively lower partial charge due to the PNP ligand, compared to  $\text{Fe}^{2+}$  with neutral ligands. Therefore, some extra electron charges of  $\text{Fe}^{2+}$  in Fe-PNP can be donated to  $\text{CO}_2$  through the backward donation as was examined in MO analysis previously. Therefore, though  $\text{Fe}^{2+}$  is Lewis acidic, when it is combined with an electron-rich ligand such as PNP(-1), the backward donation from  $\text{Fe}^{2+}$  to  $\text{CO}_2$  can occur. Accordingly, Fe-PNP coordinated to  $\text{CO}_2$  with  $\kappa^2\text{O},\text{O}'$  mode can activate  $\text{CO}_2$  through two methods: (1) by inductively attracting the electrons from the Ni-PNP side and (2) by directly donating the electron charges from itself.

### III. CONCLUSIONS

We investigated the nature of  $\text{CO}_2$  binding on four Ni(0) complexes: 1-PP ( $\eta^2\text{-CO}_2$ ), 2-PP<sup>Me</sup>P ( $\eta^2\text{-CO}_2$ ), 3-PNP ( $\eta^1\text{-CO}_2$ ), and 4-Ni- $\text{CO}_2\text{-Fe}$  ( $\mu\text{-CO}_2\text{-}\kappa\text{C}:\kappa^2\text{O},\text{O}'$ ). The DFT calculations in the regime of B3LYP/6-31G(d) + D accurately reproduced the coordination geometries of the central metals, where PP<sup>Me</sup>P ligand induces the tetrahedral structure (Td) of Ni and PNP ligand induces planar structure (Pl). Although the ligand field theory predicts that  $\text{Ni}^0$  prefers Td, the geometry of the chelating ligand enforces the coordination geometry of metal, where PP<sup>Me</sup>P leads to Td and PNP leads to Pl. As for  $\text{CO}_2$  binding mode, normally  $\text{CO}_2$  is strongly bound to the central metal in  $\eta^2$ -mode, but planar structure of  $\text{Ni}^0$ -PNP complex prefers  $\eta^1\text{-C}$  mode.

Based on the analysis of molecular orbitals, the backward donation to LUMO of the bent  $\text{CO}_2$  is mainly responsible for the  $\text{CO}_2$  binding, which is also responsible for the degree of  $\text{CO}_2$  activation. However, the binding energy (BE), although it comes from backward donation, cannot precisely explain the degree of  $\text{CO}_2$  activation because the coordination number and the deformation of ligand do affect BE. Otherwise, the charges of  $\text{CO}_2$  show strong correlation with the charge transfer (CT) energy from the energy decomposition analysis (EDA). Compared to 1-PP and 2-PP<sup>Me</sup>P, 3-PNP shows a largely increased  $\text{CO}_2$  charge of about 0.2e due to the negatively charged [PNP]<sup>-</sup> ligand.  $\text{Ni}^0$  with the coordination to PNP is already in an electron-rich state, so it can activate any adsorbate such as  $\text{CO}_2$ . In the diatomic complex of 4-Ni- $\text{CO}_2\text{-Fe}$ , an additional charge transfer of about 0.2e occurs. Interestingly, after the coordination of Fe-PNP to 3-PNP with  $\kappa^2\text{O},\text{O}'$  mode, Fe(II) pulls the electron density from Ni-PNP across the  $\text{CO}_2$  bridge, which enhances the backward donation from Ni-PNP to  $\text{CO}_2$ . Furthermore, Fe(II) also donates some charge from itself to  $\text{CO}_2$  through the backward donation mechanism. So, the resultant increased charge on  $\text{CO}_2$  comes partly from the inductive effect of Fe(II) and partly from the backward donation ascribed to PNP in Fe-PNP complex. Therefore, this finding gives insight to designing a new catalyst and explains why we should aim at the diatomic catalyst for  $\text{CO}_2$  reduction.

### ■ ASSOCIATED CONTENT

#### SI Supporting Information

The Supporting Information is available free of charge at <https://pubs.acs.org/doi/10.1021/acsomega.0c06257>.

The details of the geometry of models, MO levels of Ni(0) atom, ligands, and models, multiplicity of  $\text{Ni}^0$  and  $\text{Fe}^{2+}$  and their complexes, BE and SCF of EDA, and NBO analysis (PDF)

### ■ AUTHOR INFORMATION

#### Corresponding Author

Joonho Park – Department of Chemistry, Korea Advanced Institute of Science and Technology (KAIST), Daejeon 34141, Republic of Korea; [orcid.org/0000-0001-6642-3805](https://orcid.org/0000-0001-6642-3805); Email: [hopefulp@kaist.ac.kr](mailto:hopefulp@kaist.ac.kr)

#### Authors

Moses Cho – Neutron Science Division, Korea Atomic Energy Research Institute (KAERI), Daejeon 34057, Republic of Korea

Young Min Rhee – Department of Chemistry, Korea Advanced Institute of Science and Technology (KAIST), Daejeon 34141, Republic of Korea; [orcid.org/0000-0002-2392-3962](https://orcid.org/0000-0002-2392-3962)

Yousung Jung – Department of Chemical and Biomolecular Engineering, Korea Advanced Institute of Science and Technology (KAIST), Daejeon 34141, Republic of Korea; [orcid.org/0000-0003-2615-8394](https://orcid.org/0000-0003-2615-8394)

Complete contact information is available at: <https://pubs.acs.org/doi/10.1021/acsomega.0c06257>

#### Notes

The authors declare no competing financial interest.

### ■ ACKNOWLEDGMENTS

This research was supported by the Basic Science Research Program through the National Research Foundation of Korea (NRF) funded by the Ministry of Education (2018R1D1A1B07049044 and 2019R1A6A1A10073887). The generous supercomputing time provided by KISTI is gratefully acknowledged.

### ■ REFERENCES

- <https://www.climate.gov/> (12, 01, 2020).
- Liu, Q.; Wu, L.; Jackstell, R.; Beller, M. Using carbon dioxide as a building block in organic synthesis. *Nat. Commun.* **2015**, *6*, 5933–5933.
- Koppenol, W. H.; Rush, J. D. Reduction potential of the carbon dioxide/carbon dioxide radical anion: a comparison with other C1 radicals. *J. Phys. Chem.* **1987**, *91*, 4429–4430.
- Gibson, D. H. The Organometallic Chemistry of Carbon Dioxide. *Chem. Rev.* **1996**, *96*, 2063–2096.
- Liu, J. Catalysis by Supported Single Metal Atoms. *ACS Catal.* **2017**, *7*, 34–59.
- Álvarez, A.; Borges, M.; Corral-Pérez, J. J.; Olcina, J. G.; Hu, L.; Cornu, D.; Huang, R.; Stoian, D.; Urakawa, A.  $\text{CO}_2$  Activation over Catalytic Surfaces. *ChemPhysChem* **2017**, *18*, 3135–3141.
- Bonin, J.; Maurin, A.; Robert, M. Molecular catalysis of the electrochemical and photochemical reduction of  $\text{CO}_2$  with Fe and Co metal based complexes. Recent advances. *Coord. Chem. Rev.* **2017**, *334*, 184–198.
- Song, J.; Klein, E. L.; Neese, F.; Ye, S. The Mechanism of Homogeneous  $\text{CO}_2$  Reduction by Ni(cyclam): Product Selectivity, Concerted Proton–Electron Transfer and C–O Bond Cleavage. *Inorg. Chem.* **2014**, *53*, 7500–7507.
- Beley, M.; Collin, J. P.; Ruppert, R.; Sauvage, J. P. Electrocatalytic reduction of carbon dioxide by nickel cyclam<sup>2+</sup> in water: study of the factors affecting the efficiency and the selectivity of the process. *J. Am. Chem. Soc.* **1986**, *108*, 7461–7467.
- Beley, M.; Collin, J.-P.; Ruppert, R.; Sauvage, J.-P. Nickel(II)-cyclam: an extremely selective electrocatalyst for reduction of  $\text{CO}_2$  in water. *J. Chem. Soc., Chem. Commun.* **1984**, *0*, 1315–1315.

- (11) Craig, C. A.; Spreer, L. O.; Otvos, J. W.; Calvin, M. Photochemical reduction of carbon dioxide using nickel tetraazamacrocycles. *J. Phys. Chem.* **1990**, *94*, 7957–7960.
- (12) Froehlich, J. D.; Kubiak, C. P. Homogeneous CO<sub>2</sub> Reduction by Ni(cyclam) at a Glassy Carbon Electrode. *Inorg. Chem.* **2012**, *51*, 3932–3934.
- (13) Aresta, M.; Nobile, C. F.; Albano, V. G.; Forni, E.; Manassero, M. New nickel–carbon dioxide complex: synthesis, properties, and crystallographic characterization of (carbon dioxide)-bis-(tricyclohexylphosphine)nickel. *J. Chem. Soc., Chem. Commun.* **1975**, *0*, 636–637.
- (14) Anderson, J. S.; Iluc, V. M.; Hillhouse, G. L. Reactions of CO<sub>2</sub> and CS<sub>2</sub> with 1,2-Bis(di-tert-butylphosphino)ethane Complexes of Nickel(0) and Nickel(I). *Inorg. Chem.* **2010**, *49*, 10203–10207.
- (15) Bianchini, C.; Mealli, C.; Meli, A.; Sabat, M. Metal-promoted transformation of carbon dioxide into carbon monoxide. X-ray crystal structure of the nickel-carbonate complex [O=PPh<sub>2</sub>CH<sub>2</sub>C(CH<sub>3</sub>)-(CH<sub>2</sub>PPh<sub>2</sub>)<sub>2</sub>]Ni(O<sub>2</sub>CO).0.5H<sub>2</sub>O.C<sub>6</sub>H<sub>6</sub>. *Inorg. Chem.* **1984**, *23*, 2731–2732.
- (16) Kim, Y.-E.; Kim, J.; Lee, Y. Formation of a nickel carbon dioxide adduct and its transformation mediated by a Lewis acid. *Chem. Commun. (Cambridge, U. K.)* **2014**, *50*, 11458–11461.
- (17) Yoo, C.; Lee, Y. Formation of a tetranickel octacarbonyl cluster from the CO<sub>2</sub> reaction of a zero-valent nickel monocarbonyl species. *Inorg. Chem. Front.* **2016**, *3*, 849–855.
- (18) Yoo, C.; Lee, Y. Carbon dioxide binding at a Ni/Fe center: synthesis and characterization of Ni(η<sup>1</sup>-CO<sub>2</sub>-κC) and Ni-μ-CO<sub>2</sub>-κC:κ<sup>2</sup>O,O'-Fe. *Chem. Sci.* **2017**, *8*, 600–605.
- (19) Yoo, C.; Oh, S.; Kim, J.; Lee, Y. Transmethylation of a four-coordinate nickel(i) monocarbonyl species with methyl iodide. *Chem. Sci.* **2014**, *5*, 3853–3858.
- (20) Mankad, N. P.; Rivard, E.; Harkins, S. B.; Peters, J. C. Structural Snapshots of a Flexible Cu<sub>2</sub>P<sub>2</sub> Core that Accommodates the Oxidation States Cu<sup>I</sup>Cu<sup>I</sup>, Cu<sup>I.5</sup>Cu<sup>1.5</sup>, and Cu<sup>II</sup>Cu<sup>II</sup>. *J. Am. Chem. Soc.* **2005**, *127*, 16032–16033.
- (21) Adhikari, D.; Mossin, S.; Basuli, F.; Dible, B. R.; Chipara, M.; Fan, H.; Huffman, J. C.; Meyer, K.; Mindiola, D. J. A Dinuclear Ni(I) System Having a Diradical Ni<sub>2</sub>N<sub>2</sub> Diamond Core Resting State: Synthetic, Structural, Spectroscopic Elucidation, and Reductive Bond Splitting Reactions. *Inorg. Chem.* **2008**, *47*, 10479–10490.
- (22) Ribbe, M. W. Insights into the Mechanism of Carbon Monoxide Dehydrogenase at Atomic Resolution. *Angew. Chem., Int. Ed.* **2015**, *54*, 8337–8339.
- (23) Can, M.; Armstrong, F. A.; Ragsdale, S. W. Structure, Function, and Mechanism of the Nickel Metalloenzymes, CO Dehydrogenase, and Acetyl-CoA Synthase. *Chem. Rev.* **2014**, *114*, 4149–4174.
- (24) Lao, K. U.; Herbert, J. M. Accurate and Efficient Quantum Chemistry Calculations for Noncovalent Interactions in Many-Body Systems: The XSAPT Family of Methods. *J. Phys. Chem. A* **2015**, *119*, 235–252.
- (25) Shao, Y.; Gan, Z.; Epifanovsky, E.; Gilbert, A. T. B.; Wormit, M.; Kussmann, J.; Lange, A. W.; Behn, A.; Deng, J.; Feng, X.; Ghosh, D.; Goldey, M.; Horn, P. R.; Jacobson, L. D.; Kaliman, I.; Khaliullin, R. Z.; Kuś, T.; Landau, A.; Liu, J.; Proynov, E. I.; Rhee, Y. M.; Richard, R. M.; Rohrdanz, M. A.; Steele, R. P.; Sundstrom, E. J.; Woodcock, H. L.; Zimmerman, P. M.; Zuev, D.; Albrecht, B.; Alguire, E.; Austin, B.; Beran, G. J. O.; Bernard, Y. A.; Berquist, E.; Brandhorst, K.; Bravaya, K. B.; Brown, S. T.; Casanova, D.; Chang, C.-M.; Chen, Y.; Chien, S. H.; Closser, K. D.; Crittenden, D. L.; Diedenhofen, M.; DiStasio, R. A.; Do, H.; Dutoi, A. D.; Edgar, R. G.; Fatehi, S.; Fusti-Molnar, L.; Ghysels, A.; Golubeva-Zadorozhnaya, A.; Gomes, J.; Hanson-Heine, M. W. D.; Harbach, P. H. P.; Hauser, A. W.; Hohenstein, E. G.; Holden, Z. C.; Jagau, T.-C.; Ji, H.; Kaduk, B.; Khistyayev, K.; Kim, J.; Kim, J.; King, R. A.; Klunzinger, P.; Kosenkov, D.; Kowalczyk, T.; Krauter, C. M.; Lao, K. U.; Laurent, A. D.; Lawler, K. V.; Levchenko, S. V.; Lin, C. Y.; Liu, F.; Livshits, E.; Lochan, R. C.; Luenser, A.; Manohar, P.; Manzer, S. F.; Mao, S.-P.; Mardirossian, N.; Marenich, A. V.; Maurer, S. A.; Mayhall, N. J.; Neuscamman, E.; Oana, C. M.; Olivares-Amaya, R.; O'Neill, D. P.; Parkhill, J. A.; Perrine, T. M.; Peverati, R.; Prociuk, A.; Rehn, D. R.; Rosta, E.; Russ, N. J.; Sharada, S. M.; Sharma, S.; Small, D. W.; Sodt, A.; Stein, T.; Stück, D.; Su, Y.-C.; Thom, A. J. W.; Tsuchimochi, T.; Vanovschi, V.; Vogt, L.; Vydrov, O.; Wang, T.; Watson, M. A.; Wenzel, J.; White, A.; Williams, C. F.; Yang, J.; Yeganeh, S.; Yost, S. R.; You, Z.-Q.; Zhang, I. Y.; Zhang, X.; Zhao, Y.; Brooks, B. R.; Chan, G. K. L.; Chipman, D. M.; Cramer, C. J.; Goddard, W. A.; Gordon, M. S.; Hehre, W. J.; Klamt, A.; Schaefer, H. F.; Schmidt, M. W.; Sherrill, C. D.; Truhlar, D. G.; Warshel, A.; Xu, X.; Aspuru-Guzik, A.; Baer, R.; Bell, A. T.; Besley, N. A.; Chai, J.-D.; Dreuw, A.; Dunietz, B. D.; Furlani, T. R.; Gwaltney, S. R.; Hsu, C.-P.; Jung, Y.; Kong, J.; Lambrecht, D. S.; Liang, W.; Ochsenfeld, C.; Rassolov, V. A.; Slipchenko, L. V.; Subotnik, J. E.; van Voorhis, T.; Herbert, J. M.; Krylov, A. I.; Gill, P. M. W.; Head-Gordon, M. Advances in molecular quantum chemistry contained in the Q-Chem 4 program package. *Mol. Phys.* **2014**, *113*, 184–215.
- (26) Glendening, E. D.; Badenhop, J. K.; Reed, A. E.; Carpenter, J. E.; Bohmann, J. A.; Morales, C. M.; Weinhold, F. *NBO 7.0 PROGRAM CITATION*; University of Wisconsin, Madison (2018) [http://nbo6.chem.wisc.edu/biblio\\_css.htm](http://nbo6.chem.wisc.edu/biblio_css.htm) (12, 01, 2020).
- (27) Khaliullin, R. Z.; Cobar, E. A.; Lochan, R. C.; Bell, A. T.; Head-Gordon, M. Unravelling the Origin of Intermolecular Interactions Using Absolutely Localized Molecular Orbitals. *J. Phys. Chem. A* **2007**, *111*, 8753–8765.
- (28) Galan, F.; Fouassier, M.; Tranquille, M.; Mascetti, J.; Pápai, I. CO<sub>2</sub> Coordination to Nickel Atoms: Matrix Isolation and Density Functional Studies. *J. Phys. Chem. A* **1997**, *101*, 2626–2633.
- (29) Kégl, T.; Ponec, R.; Kollár, L. Theoretical Insights into the Nature of Nickel–Carbon Dioxide Interactions in Ni(PH<sub>3</sub>)<sub>2</sub>(η<sup>2</sup>-CO<sub>2</sub>). *J. Phys. Chem. A* **2011**, *115*, 12463–12473.